materials

MDPI

Article

HTPFA-Coated AlB_2 with Enhanced Combustion Performance as a High-Energy Fuel

Jiangfeng Wang, Wanjun Zhao *, Chen Shen, Yapeng Ou and Qingjie Jiao

State Key Laboratory of Explosion Science and Technology, Beijing Institute of Technology, Beijing 100081, China; wangjiangfength@163.com (J.W.); shenchen1638@163.com (C.S.); ouyapeng@bit.edu.cn (Y.O.); jqj@bit.edu.cn (Q.J.)
* Correspondence: wanjunzhaowj@bit.edu.cn

Abstract: High-energy boron-based fuel aluminum-diboride (AlB_2) has attracted much attention in the field of solid propellants. However, the low reactivity of AlB_2 hindered its further application. In this study, highly reactive AlB_2@hydroxyl-terminated perfluoropolyether alcohol (AlB_2@HTPFA) composites with a core–shell structure were prepared by coating AlB_2 with functionalized fluoropolymers by using a facile one-step in situ polymerization method. AlB_2@HTPFA composites with varying polymer contents (0, 5, 10, and 15 wt%) were obtained. The in situ polymerization strategy enables precise control over the polymer coating thickness and interfacial interactions, which is critical for optimizing the reactivity and thermal stability of composites. The morphology and structure were characterized, and the microcore–shell structure of AlB_2@HTPFA was obtained. Compared with raw AlB_2, the combustion efficiency of coated fuel increased by 4.1%, 5.6%, and 7.5%, respectively, with varying polymer contents. Meanwhile, the reactivity of AlB_2@HTPFA (5 wt%) was 0.65 MPa/s, which is ~1.5 times that of AlB_2. Additionally, the ignition and combustion characteristics of AlB_2@HTPFA were investigated by laser ignition experiments with potassium perchlorate (KP) as an oxidant. The results revealed that AlB_2@HTPFA/KP composites showed a greatly reduced combustion duration compared to uncoated AlB_2. The ignition and combustion enhancement mechanism of AlB_2@HTPFA was proposed. During the ignition process, the existence of HTPFA can result in a pre-ignition reaction, thus raising its reaction activity. This work provided a promising candidate for high-energy fuel that can be used in energetic materials.

Keywords: AlB_2; functionalized fluoropolymer; ignition; combustion characteristic; preignition reaction

check for updates

Academic Editor: Yuwen Chen

Received: 22 February 2025
Revised: 17 March 2025
Accepted: 22 March 2025
Published: 25 March 2025

Citation: Wang, J.; Zhao, W.; Shen, C.; Ou, Y.; Jiao, Q. HTPFA-Coated AlB_2 with Enhanced Combustion Performance as a High-Energy Fuel. *Materials* **2025**, *18*, 1452. https://doi.org/10.3390/ma18071452

Copyright: © 2025 by the authors. Licensee MDPI, Basel, Switzerland. This article is an open access article distributed under the terms and conditions of the Creative Commons Attribution (CC BY) license (https://creativecommons.org/licenses/by/4.0/).

1. Introduction

AlB_2, a boron-based compound, has attracted large amounts of interests for application in energetic materials due to its higher volumetric heat of 122–140 kJ/cm^3, higher energy release rate, and higher combustion efficiency [1–5] compared with one of boron [6–8]. Moreover, AlB_2 could reduce the ignition delay of high-energy formulations by 2–2.5 times [9,10]. However, during the combustion of AlB_2, B_2O_3 with a low melting point (450 °C) and a high boiling point (1860 °C) [11] emerged as an impervious liquid film on the surface, preventing AlB_2 contacting with oxygen and thus reducing combustion efficiency in the initial stages. It has been reported that the combustion characteristics of boron-containing fuels could be improved by changing their surface chemicals [12–14]. To the best of our knowledge, there were few studies about the coating of AlB_2. Currently, fluorine-containing organic compounds (FCOCs), particularly polymers rich in fluorine, are interesting candidates for being

employed as energetic additives [15,16]. In the realm of energy materials, FCOC-containing substable hybrid composites have drawn more and more attention recently. According to the reported literature [17–20], FCOCs were frequently added to materials containing aluminum to enhance the ignition and combustion performance. It can be attributed to the fact that fluoropolymers, acting as oxidizing agents, could stimulate surface exothermic reactions between the alumina shells and fluorine, thus enhancing ignition and combustion [21–23]. Wang et al. [24] conducted a comparative study of the ignition and combustion properties of Al-PVDF, Al-Viton (hexafluoropropylene and vinylidene fluoride), and Al-THV (tetrafluoroethylene, hexafluoropropylene, and vinylidene fluoride), revealing that the content of fluorine played an important role in determining the combustion characteristics of energetic composites. In contrast to coating B with metal and organic chemicals, fluorine-containing materials could also be utilized [25]. Fluorinated modification materials for boron-based fuels primarily include metal fluorides, fluorinated graphene, and fluoropolymers. Current studies on fluoropolymer coatings for boron-based fuels, including trifluoroethylene-HFP copolymer (Viton A) [26], trifluoroethylene-HFP copolymer (THF) [27], polyvinylidene fluoride (PVDF) [28], and polytetrafluoroethylene (PTFE) [29], demonstrate their capacity to reduce ignition delay, improve combustion duration, and enhance combustion efficiency. This performance enhancement arises partly from the fluorination reaction where B_2O_3 reacts with fluorine to form BF_3 releasing 188.99 kcal/m^3 [30–32]—which promotes boron oxidation kinetics [28,33], thereby enabling fluorine-containing polymers to optimize boron combustion. However, there were insufficient data stating the mechanism of the effect of fluorinated oxides on the energetic behavior of AlB_2.

Fluoropolymers could be introduced into the system through chemical and physical methods. Viton A, THF, and PVDF are typically coated via recrystallization methods, whereas PTFE coatings are prepared through high-energy ball milling combined with recrystallization. Beyond these approaches, electrospinning [34,35] represents another common yet relatively complex fabrication process for fluoropolymer coatings. Usually, linking organic fluorine to the molecular network structure with chemical reaction could be clarified as the chemical method, for instance, end-hydroxy fluoroelastomer cured with isocyanate, end-carboxy fluoroelastomer cured with epoxy resin [36], and the fluorine modification of adhesive followed by curing agent reaction [37–39]. Considering the high fluorine content, inertia, and liquid state at room temperature, HTPFA was chosen as the fluorine-containing organic substance for the study of AlB_2 [40,41]. Additionally, the hydroxyl group on the alcohol can be grafted into the adhesive network by reacting with the isocyanate group in the curing agent, improving the stability [42,43]. Notably, this study pioneers the selection of HTPFA as a fluoropolymer for coating AlB_2 via a one-step in situ polymerization method. To the best of our knowledge, the coating of AlB_2 with PFA has been implemented for the first time.

In this work, the AlB_2 colloid was modified through the addition of specified amounts of HTPFA and poly(1,6-diisocyanatohexane) (N_{100}) curing agent, utilizing a one-step in situ polymerization method. The morphology, thermal characteristics, ignition, and combustion characteristics of coated AlB_2 were examined and compared with those of AlB_2. In addition, the function of the HTPFA polymers in the combustion of AlB_2 was clarified, which displayed guidance to utilize AlB_2@HTPFA as a new high-energy fuel in energetic materials.

2. Materials and Methods

2.1. Materials

The raw AlB_2 with a median particle size of 7.9 μm was supplied from Tangshan Weihao Magnesium Powder Co., Ltd. (Qian'an City, China) and manufactured by sintering technique before being used. The impurities were mostly unreacted with Al. N_{100} was

brought from Shanghai McLean Biochemical Science and Technology Co., Ltd. (Shanghai, China). HTPFA was provided by Jiangsu Aikang Biomedical Research and Development Co., Ltd. (Nanjing, China). Butyl dilaurate (T_{12}) with a purity of 95% as catalyst was acquired from Beijing Tongguang Fine Chemical Company (Beijing, China). The acetone used as the dispersion of N_{100} with an HPLC purity of 99.7% was provided by Beijing Tongguang Fine Chemical Company. The potassium perchlorate ($KClO_4$) with a purity of 99.99%, employed as an oxidizer for laser ignition, was provided by Aladdin Company. For the laser ignition tests, $KClO_4$ was selected as the oxidizing agent since it was a significant oxidant employed in the development of composites with impact safety [44,45].

2.2. Sample Preparation

To investigate the effect of HTPFA content on the properties of AlB_2, three types of coated AlB_2 with HTPFA mass ratios of 5 wt%, 10 wt%, and 15 wt% were prepared, respectively. The detailed preparation steps are as follows.

Firstly, a specific amount of N_{100} was added into the mixture of HTPFA and AlB_2, which had been dissolved in the acetone under magnetic stirring. Secondly, a specific amount of T_{12} was added dropwise, which was followed by further magnetic stirring for three hours at room temperature. After filtration, washing, and drying at 55 °C for three hours, three different types of coated AlB_2 were eventually obtained due to the reaction generating carbamate between the hydroxyl group on HTPFA and the isocyanate on N_{100}. AlB_2@HTPFA-5, AlB_2@HTPFA-10, and AlB_2@HTPFA-15 were the corresponding notations. The mass ratio of the two components of the composites AlB_2@HTPFA was calculated using simulations of complete oxidation reactions, and the composites utilized in the laser ignition tests were made by physically combining for 30 min, 50 wt% of AlB_2@HTPFA, and 50 wt% of $KClO_4$.

2.3. Characterizations

A scanning electron microscope (SEM, SU8020, Hitachi, Tokyo, Japan) and an energy dispersive spectrometer (EDS) were used to analyze the morphology and elemental distribution of AlB_2 and AlB_2@HTPFA. The particle size distribution of AlB_2@HTPFA was analyzed by a laser particle size analyzer (Malvern Mastersizer 2000, Malvern Panalytical, Malvern, UK). The crystalline phase of AlB_2 and AlB_2@HTPFA was analyzed by X-ray diffraction (XRD, D8 ADVANCE, BRUCKER, Karlsruhe, Germany) at 40 kV/40 mA, with a 2θ range of 5–90° in the pace of 0.02°/0.1 s. AlB_2 and AlB_2@HTPFA were subjected to XPS experiments using X-ray photoelectron spectroscopy (XPS, Escalab 250Xi, Thermo, Waltham, MA, USA).

Thermogravimetric analysis (TGA) and differential scanning calorimetry (DSC, STA449F3, NETZSCH, Selb, Germany) were simultaneously conducted to investigate the thermal reaction behaviors of the AlB_2 and AlB_2 @HTPFA. The sample of about 3 mg was heated from 25 °C to 1200 °C in an air atmosphere (50 mL/min) at a heating rate of 10 °C/min. The samples were analyzed using Bruker VERTEX 70 (Rosenheim, Germany) and Netzsch STA 449 F3 (Selb, Germany)-coupled thermogravimetric-Fourier transform infrared spectroscopy (TG-FTIR) analysis in which the sample of about 3 mg was heated from room temperature to 1000 °C in air atmosphere (50 mL/min) with a heating rate of 10 °C/min, while the FTIR spectral analysis ran. The scanning range of the FTIR detector was 4000~400 cm^{-1} with a resolution of 4 cm^{-1}. A microcomputer automated calorimeter (MAC, TRHW-7000C, Hebi Tianrun Electronic Technology Co., Ltd., Hebi, China) was used to determine the calorific value of AlB_2 and AlB_2 @HTPFA. In this experiment, approximately 0.2 g of the samples was put into the calorimeter inflated with oxygen under 3 MPa, and the heat release was measured.

A constant volume combustion cell test of 30 mg of samples was conducted by the flame ignition method with an oxygen atmosphere (~3 MPa) to characterize the energy response and work capacity of the AlB_2 and AlB_2@HTPFA. The flame was generated by the tip of a nichrome wire, which was heated by a controlled DC current. The sensor recorded the changes in pressure during the vigorous oxidation process with time, and the measurements were repeated three times for each sample and averaged. Laser ignition experiments were used to assess the ignition combustion process of AlB_2 and AlB_2@HTPFA. The samples were ignited by a carbon dioxide laser (Shanghai Yuhong Laser Equipment Co., Ltd., Shanghai, China), and the flame was filmed at 8000 fps using a high-speed video camera (X113). The ignition power and ignition time were adjusted to 50 W and 500 ms, respectively. To study the combustion process of the particles using high-speed pictures, 30 mg of mechanically mixed samples was fired in the air and placed in the center of the ignition table.

3. Results and Discussion

3.1. Characterization of Morphology and Components

The microstructure of AlB_2 and AlB_2@HTPFA was examined by SEM, and the morphology was shown in Figure 1. The majority of the raw AlB_2 was irregular particles, while the AlB_2@HTPFA particles were equally dispersed with no visible agglomeration. In comparison to the raw AlB_2, as the content of the surface coating increased, the surface of AlB_2@HTPFA gradually became smooth, demonstrating that the surface morphology of AlB_2 might be altered by controlling the HTPFA polymer content.

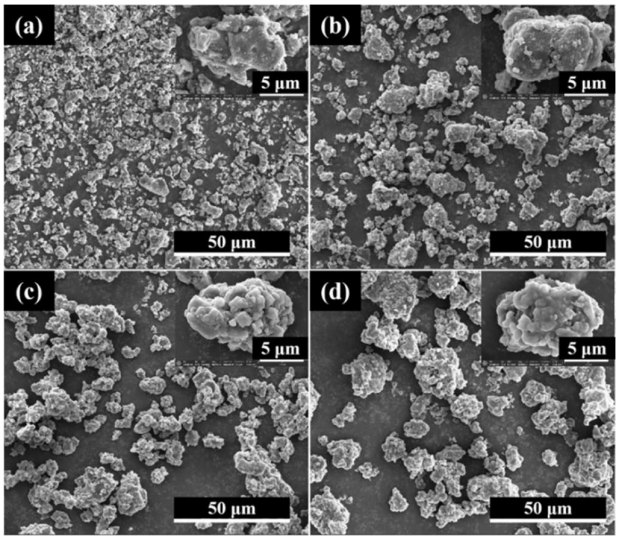


Figure 1. SEM images of (**a**) AlB_2, (**b**) AlB_2@HTPFA-5, (**c**) AlB_2@HTPFA-10, and (**d**) AlB_2@HTPFA-15.

The EDS results in Figure 2a indicated that the Al, B, and O elements were distributed evenly on the surface of AlB_2, confirming the presence of oxide shells. In addition to Al, B, and O, the surface of the AlB_2@HTPFA in Figure 2b–d was uniformly distributed with F elements, verifying that the HTPFA polymer was uniformly distributed on the surface of AlB_2, proving the feasibility of the preparation method. The quantitative analysis results from EDS have been added to the Supporting Information (Table S1). The data reveal a gradual increase in surface F content with higher coating ratios, which conclusively confirms the successful coating of AlB_2 by HTPFA.

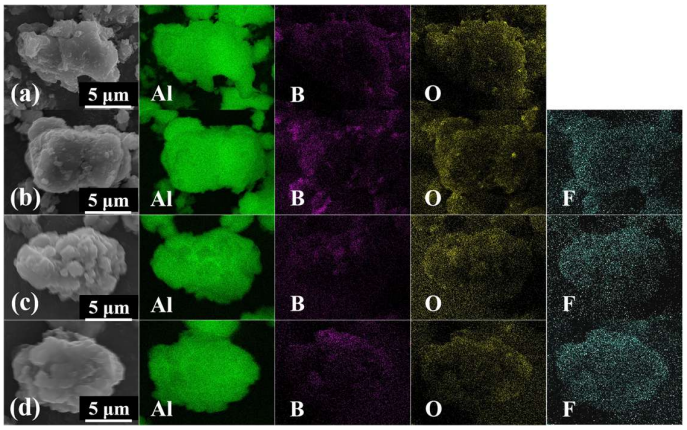


Figure 2. EDS images of (**a**) AlB_2, (**b**) AlB_2@HTPFA-5, (**c**) AlB_2@HTPFA-10, and (**d**) AlB_2@HTPFA-15.

Additionally, a laser particle size analyzer was used to characterize the particle size distribution of AlB_2@HTPFA. The particle sizes of AlB_2@HTPFA samples were regularly distributed, as illustrated in Figure 3a, and there was no evident agglomeration. The median diameters of the AlB_2@HTPFA particles were 8.55 μm, 8.94 μm, and 9.22 μm, respectively, which is larger than that of the pristine AlB_2 (7.9 μm), which demonstrates the feasibility of comparing the performances of AlB_2 and AlB_2@HTPFA. The XRD patterns of AlB_2 and AlB_2@HTPFA in Figure 3b revealed that the raw AlB_2 was composed of Al and AlB_2, and the presence of oxide shells was not detected since the oxide shell is amorphous. The crystalline composition of AlB_2@HTPFA was identical to that of the AlB_2, indicating that there was no change in the crystal structure of AlB_2 during the preparation of the AlB_2@HTPFA samples. There is no appearance of HTPFA patterns due to its amorphous form.

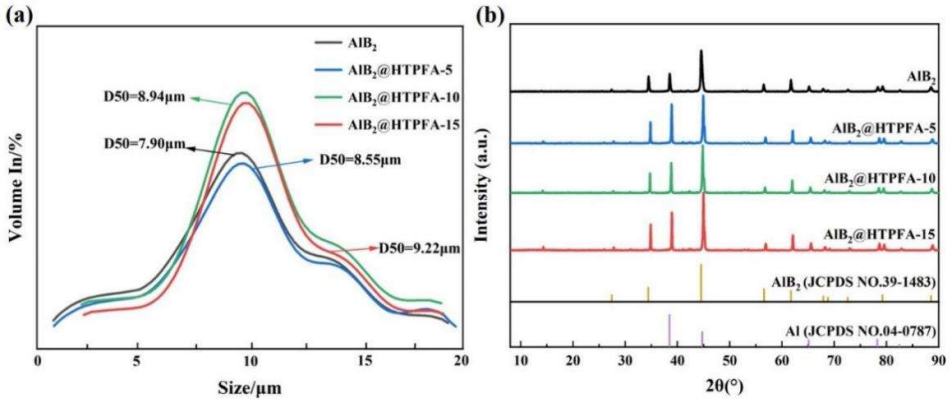


Figure 3. Particle size distribution curve (**a**) and XRD patterns (**b**) of AlB_2 and AlB_2@HTPFA.

To clarify the adsorption form of polymers on the surface of AlB_2, an XPS of AlB_2@HTPFA-10 was conducted [46]. As shown in Figure 4, the interface contact form between AlB_2 and HTPFA was characterized, and the Al 2s, O 1s, C 1s, and F 1s peaks can be observed, which indicates the successful coating of HTPFA on AlB_2 for AlB_2@HTPFA-10.

The chemical states of Al, B, O, and F in AlB_2@HTPFA-10 were investigated using split-peak fitting (Figure 5), which revealed C-O bonds (531.8 eV) and two O-F bonds (535.7 eV) in the O 1s peaks (536.8 eV), and two peaks (688.15 eV) with C-F bonds (689.1 eV) in the F 1s spectra, originated from HTPFA. There were no new Al-F or B-F bonds formed, indicating that the polymer was physically adsorbed on the surface of AlB_2.

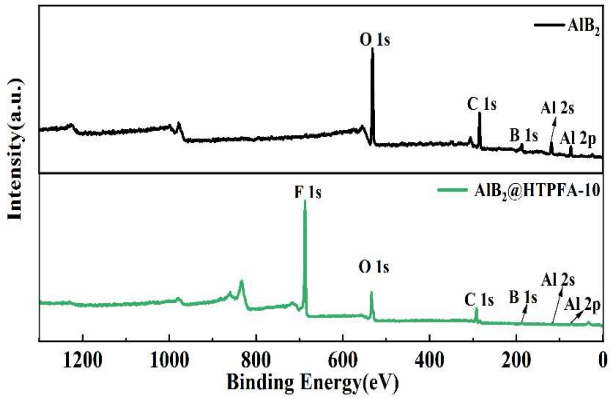


Figure 4. XPS spectra of AlB_2 and AlB_2@HTPFA-10.

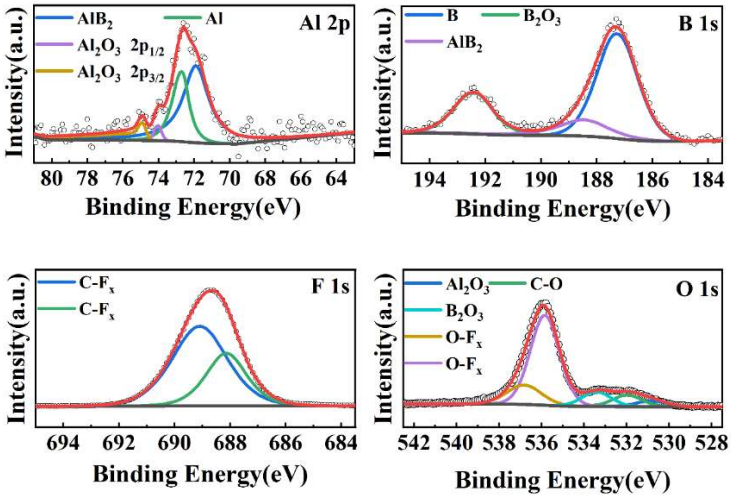


Figure 5. XPS spectra of Al 2p peaks, B 1s peaks, F 1s peaks, and O 1s peaks for AlB_2@HTPFA-10.

The XRD results of pristine AlB_2 (Figure 3b) show diffraction peaks corresponding only to crystalline Al (PDF#04-0787) and AlB_2 (PDF#65-2351), with no detectable diffraction peaks for aluminum oxide or boron oxide. This confirms the amorphous nature of the oxide shell (e.g., Al_2O_3 and B_2O_3), as XRD is only sensitive to crystalline phases. The XPS B 1s spectrum (Figure 5) reveals a weak peak at 187.5 eV, attributed to B-O bonds, indicating trace surface oxidation. However, the oxide layer thickness is insufficient to form a crystalline phase. After HTPFA coating, the intensity of the B-O peak decreases significantly, demonstrating the coating's ability to suppress oxidation.

3.2. Oxidation Process

TGA and DSC were used to investigate the oxidation process of AlB_2 and AlB_2@HTPFA in air. The DSC and TG curves shown in Figure 6 display that the reaction process of the AlB_2@HTPFA samples can be divided into three stages based on mass changes: the decomposition of polymer (stage I), the initial oxidation of AlB_2 (stage II), and the AlB_2 decomposition oxidation reaction (stage III). There was no first-stage response observed in the curves of AlB_2. The TGA/DSC curves of HTPFA have been added to the Supporting Information (Figure S1), and the TGA/DSC parameters have been quantified in the table (Table S2).

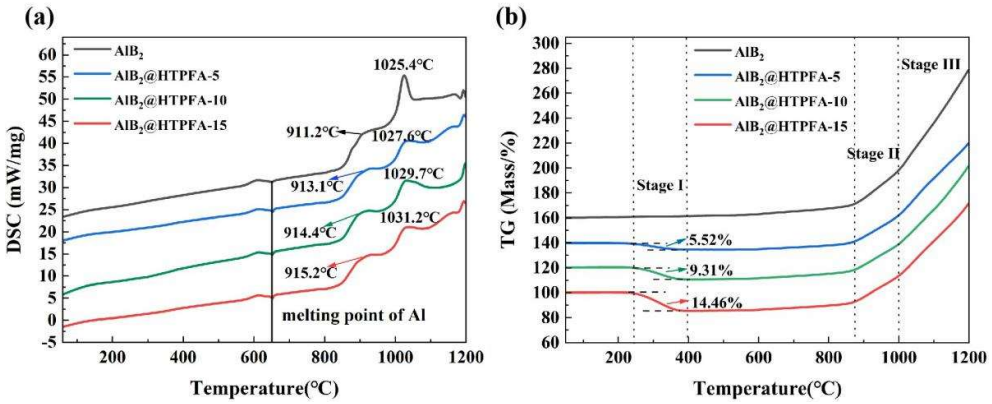


Figure 6. DSC/TG curves of AlB_2 and AlB_2@HTPFA samples: (**a**) DSC (**b**) TG.

The decomposition of the polymer ranged from 25 °C to 400 °C. The weight loss of AlB_2@HTPFA samples could be observed between 230 °C and 400 °C, indicating that polymer decomposition on the surface of the samples occurred at this temperature, and the mass loss was positively correlated with the ratio of the polymer shell. As the temperature increased, exothermic peaks developed in different samples at about 600 °C (Figure 6a), accompanied by a slow rise in mass due to the minor-quantity Al in the sample reacting with O_2 and producing Al_2O_3 (Equation (1)) [47,48]. Al melted endothermically at about 660 °C, as seen by the endothermic peak in Figure 6a. The initial oxidation of AlB_2 and AlB_2@HTPFA occurred between 880 °C and 1000 °C when AlB_2 interacted exothermically with O_2 to produce Al_2O_3 and B_2O_3 (Equation (3)), and simultaneously amorphous alumina first changed into γ-Al_2O_3 [49]. Compared with amorphous alumina, the γ-Al_2O_3 owned greater density, which created more voids in the oxide shell, increasing the oxygen diffusion rate and sample quality during this phase.

AlB_2 decomposition oxidation reaction ranged from 1000 °C to 1200 °C. At high temperatures, AlB_2 transformed into AlB_{12}, which was influenced by parameters such as ball milling time and sintering time during the sintering preparation process of raw AlB_2, corresponding to the conversion temperatures ranging from 956 ° C to 1350 °C reported by different researchers [50–52]. Endothermic peaks near 980 °C were observed in various samples (Figure 6b). Based on the temperature of AlB_{12} observed in Figure 7, the breakdown temperature of AlB_2 in this investigation was near 980 °C. The decomposition process of AlB_2 yielded a large amount of Al liquid, and, at higher temperatures, the presence of Al liquid could aid the oxidation process through rapid exothermic reactions and increased transport [48], immediately oxidizing on contact with air [53], resulting in a rapid increase in mass (Equation (4)).

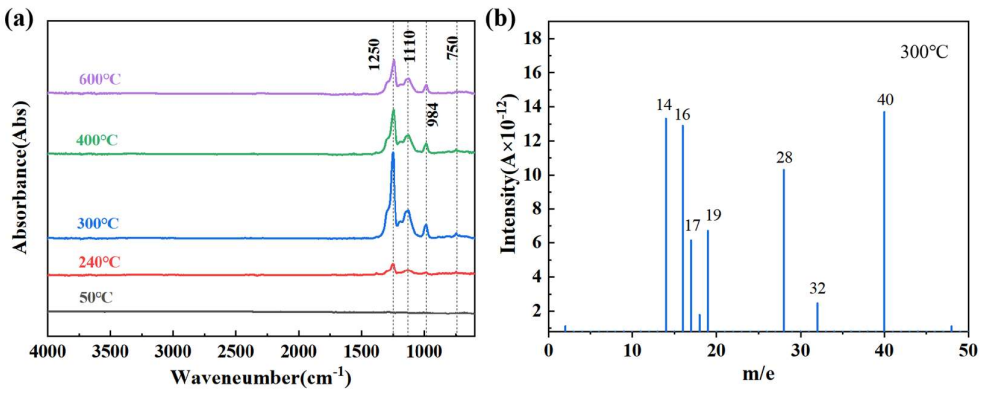


Figure 7. FTIR spectra of decomposition products of AlB_2@HTPFA-10 at different temperatures (**a**) and MS spectra of decomposition products at 300 °C (**b**).

To determine the decomposition products of AlB_2@HTPFA in the first stage, the AlB_2@HTPFA-10 was chosen for Fourier infrared testing with temperatures ranging from 25 °C to 600 °C. As the FTIR spectra of the products show in Figure 7a, the FTIR curve of the sample remained unchanged at 50 °C. At the initial decomposition temperature of 240 °C, significant absorption peaks could be observed around 1250 cm^{-1}, corresponding to the bending vibration peaks of the C-F bond. Combined with the mass-to-charge ratio (m/e) of 19 in the mass spectrometry, which may correspond to F^-, it indicates the presence of fluoride-containing compounds in the decomposition products. The appearance of these absorption peaks suggests that the polymer initially decomposes mainly into C_xF_y during the initial stage of decomposition, which is consistent with the mass loss from 25 °C to 240 °C in the thermogravimetric (TG) curve shown in Figure 6b.

When the temperature is raised to 300 °C, three new distinct absorption peaks appear at 750 cm^{-1}, 984 cm^{-1}, and 1110 cm^{-1}. Based on mass spectrometry analysis, they are, respectively, the symmetric vibration peak of the Al-F bond (750 cm^{-1}) and the stretching vibration peaks of the C-O-C ether bond [36] (984 cm^{-1} and 1110 cm^{-1}). Since no formation of Al-F or B-F bonds was found in the X-ray photoelectron spectroscopy (XPS) analysis of AlB_2@HTPFA, the appearance of the Al-F bond at this time may be due to the reaction between HF decomposed from HTPFA and the Al_2O_3 on the surface. It is worth noting that HF was not detected in the infrared spectrum. This may be because the branched structure of HTPFA reduces the release of HF, resulting in most of the decomposition products existing in the form of C-F, and the small amount of HF generated reacts immediately with the oxides. As the temperature rises, the peaks of other substances remain basically unchanged, while the peaks of C_xF_y first gradually weaken and then remain basically constant. This may be because after decomposition, some of the products react with the oxides on the surface of AlB_2, reducing the content of F^-. There are no other gas products that change significantly, indicating that the polymer decomposes completely at approximately 300 °C.

Furthermore, to determine the intermediate products of AlB_2 and modified AlB_2 in the oxidation process, the reaction products of raw AlB_2 and AlB_2@HTPFA-10 samples at three different temperatures were characterized by XRD. Figure 8 exhibited that the diffraction peaks of AlB_2 gradually weakened, and the peaks of α-Al_2O_3 began to appear in the process of the temperature approaching 1000 °C, indicating that the alumina underwent the crystalline phase transition in this process. It was suggested that in this process, the crystalline phase of alumina was changed from γ to α [47,49]. In addition, a small amount of unreacted Al remained in the product, and the AlF_3 peaks were not identified in the AlB_2@HTPFA at this temperature, owing to the small quantity of coating or the volatilization of some AlF_3. As the reaction progressed, Al_2O_3 and B_2O_3 combined to form $Al_4B_2O_9$ ($2Al_2O_3 \cdot B_2O_3$) at temperatures below 1035 °C, which decomposed to $Al_{18}B_4O_{33}$ ($9Al_2O_3 \cdot 2B_2O_3$) at higher temperatures [54,55], and the mass continued to grow. Although $Al_{18}B_4O_{33}$ occurred at higher temperatures, it cooled and changed into Al_2O_3 and $Al_{18}B_4O_{33}$ [56]; thus, the products were dominated by Al_2O_3 and $Al_4B_2O_9$ with no B_2O_3, indicating that B_2O_3 was amorphous at this point.

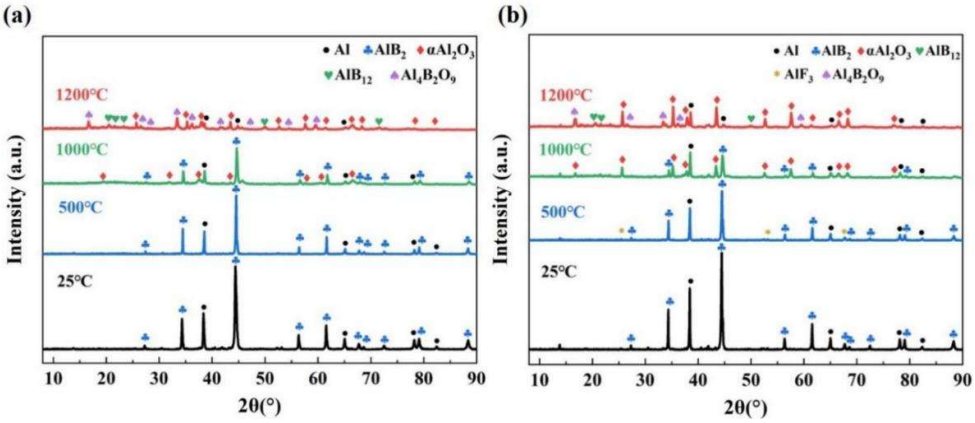


Figure 8. X-ray diffraction patterns of samples at different temperatures: (**a**) AlB_2 and (**b**) AlB_2@HTPFA-10.

The TGA curves of AlB_2@HTPFA resembled that of AlB_2. Aside from the conventional oxidation process of AlB_2, it involved the reaction of surface fluoropolymer. The overall weight gain of AlB_2, AlB_2@HTPFA-5, AlB_2@HTPFA-10, and AlB_2@HTPFA-15 during the entire reaction phase was 118.63%, 80.76%, 80.47%, and 73.39%, respectively, indicating that certain compounds remaining on the surface of AlB_2 were formed by the disintegration of the HTPFA coating layer at 400 °C. Because of the low permeability of these compounds, the oxygen transport on the surface of AlB_2 was hindered. It indicated that some of the products produced by the decomposition of the HTPFA coating layer at 400 °C remained on the surface of AlB_2. It was noted that the products showed poor breathability, which prevented the oxygen passage on the surface of AlB_2. That was why the first and second oxidation peak temperatures of AlB_2@HTPFA were more than 2 °C higher than those of AlB_2.

$$Al + 0.75O_2 \rightarrow 0.5Al_2O_3,\ \Delta H = -826.7\ kJ/mol \quad (1)$$

$$AlB_2 + 2.25O_2 \rightarrow 0.5Al_2O_3 + B_2O_3,\ \Delta H = -2241.1\ kJ/mol \quad (2)$$

$$AlB_2 \rightarrow 1/6AlB_{12} + 5/6Al,\ \Delta H = 18.9\ kJ/mol \quad (3)$$

$$AlB_{12} + 9.75O_2 \rightarrow 0.5Al_2O_3 + 6B_2O_3,\ \Delta H = -8727.1\ kJ/mol \quad (4)$$

$$Al_2O_3 + 0.5B_2O_3 \rightarrow 0.5Al_4B_2O_9,\ \Delta H = -155.6\ kJ/mol \quad (5)$$

3.3. Calorimeter and Combustion Test

To investigate the energy release of AlB_2 and AlB_2@HTPFA, the calorific value of samples was examined, and the findings are displayed in Figure 9. The heat of combustion increased initially and then decreased as the content of HTPFA increased. Due to the fact that Al produces more heat during the fluorination process (70.40 MJ/kg) compared with the oxidation process (36.29 MJ/kg) [57], AlB_2@HTPFA-5 exhibited a higher calorific value than the basic raw AlB_2. However, as the amount of the surface coating layer grows, the total calorific value drops due to the low calorific value of fluoropolymer. The results indicated that the HTPFA coating layer promoted the energy release of AlB_2, and the energy-releasing rate steadily increased by 4.1%, 5.6%, and 7.5%, respectively, with the increasing HTPFA content. Therefore, it followed that exothermic fluorination between the surface oxide shells and fluorine stimulated the overall reactivity of AlB_2, leading to a deeper degree of reactivity and improved energy efficiency of the modified AlB_2@HTPFA.

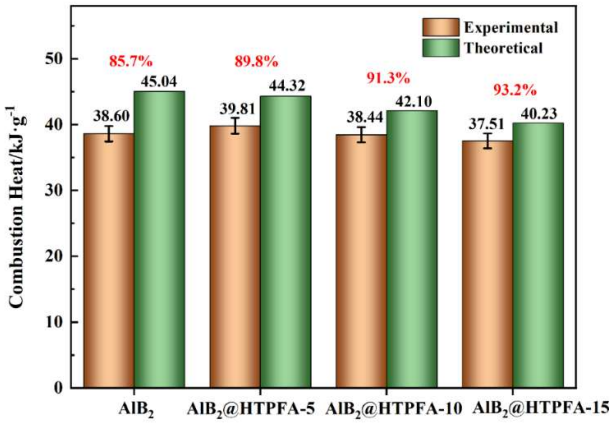


Figure 9. Test results of the calorific value and calculated energy efficiency.

The pressure change of AlB_2 and AlB_2@HTPFA with time was measured by the pressure cell. The rate of the pressure change was used to describe the vigorous oxidation process, which could be quantified as the rate of pressurization (MPa/ms), as shown in Equation (6).

Pressurization rate:

$$v = (P_{max} - P_i)/(t_{max} - t_i) \quad (6)$$

where P_{max} represents the maximum pressure, P_i represents the pressure when the ignition process begins, t_{max} represents the time until the pressure reaches its maximum value, and t_i represents the ignition time.

The peak pressure of AlB_2@HTPFA was higher than that of AlB_2, as shown in Figure 10a. Figure 10b demonstrated that the pressurization rate of AlB_2@HTPFA-5, AlB_2@HTPFA-10, and AlB_2@HTPFA-15 was all higher (0.65 MPa/s, 0.58 MPa/s, and 0.43 MPa/s, respectively) than that of AlB_2 (0.41 MPa/s). It can be attributed to the fact that during the ignition process, the surface coating layer broke down quickly and reacted with the surface oxides of AlB_2, causing an AlB_2 preignition reaction (PIR) to occur before oxidation, promoting the contact between AlB_2 and O_2, deepening the reaction degree and speeding up the reaction rate.

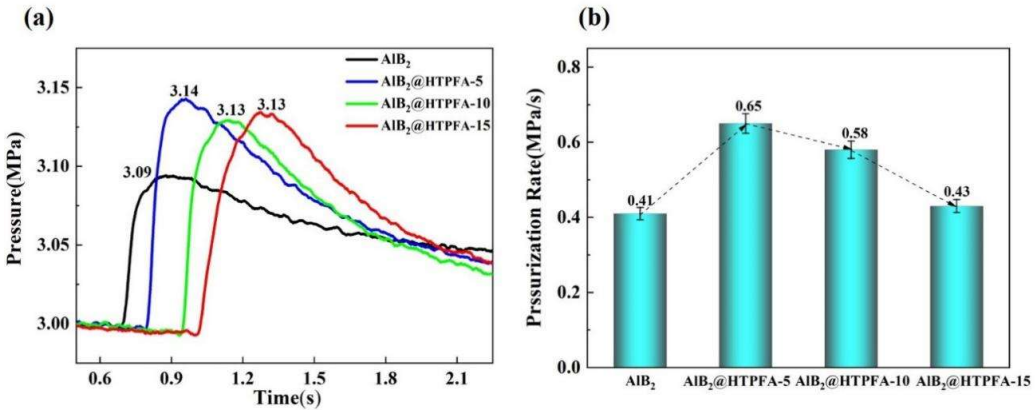


Figure 10. (**a**) The pressure changed with time and (**b**) the pressurization rate of AlB_2 and AlB_2@HTPFA.

3.4. Laser Ignition Measurement

The ignition and combustion processes of energetic materials with KP as the oxidant were characterized by a laser ignition test with results depicted in Figure 11. AlB_2/KP has a combustion time of 410.2 ms. The AlB_2@KP burned for a shorter period of time after adding the HTPFA. Compared with AlB_2/KP, AlB_2@HTPFA-5/KP, AlB_2@HTPFA-10/KP, and

AlB_2@HTPFA-15/KP exhibited reductions of 97.7 ms, 134.0 ms, and 211.9 ms, respectively. AlB_2@HTPFA-15/KP reached the maximum flame with approximately 105.8 ms, which was earlier than AlB_2@HTPFA-5/KP and produced more gaseous products, for the reason that as the content of the fluorine polymer on the surface increased, the decomposition of the fluorine polymer and oxidant produced a significant number of gaseous products in addition to the pre-ignition reaction between the oxide and fluorine polymer on the AlB_2 surface. The diffusion and reaction processes involving AlB_2 particles were accelerated. As a result, coating AlB_2 with HTPFA polymer could improve the reactivity and reduce the combustion duration of AlB_2-based energy materials.

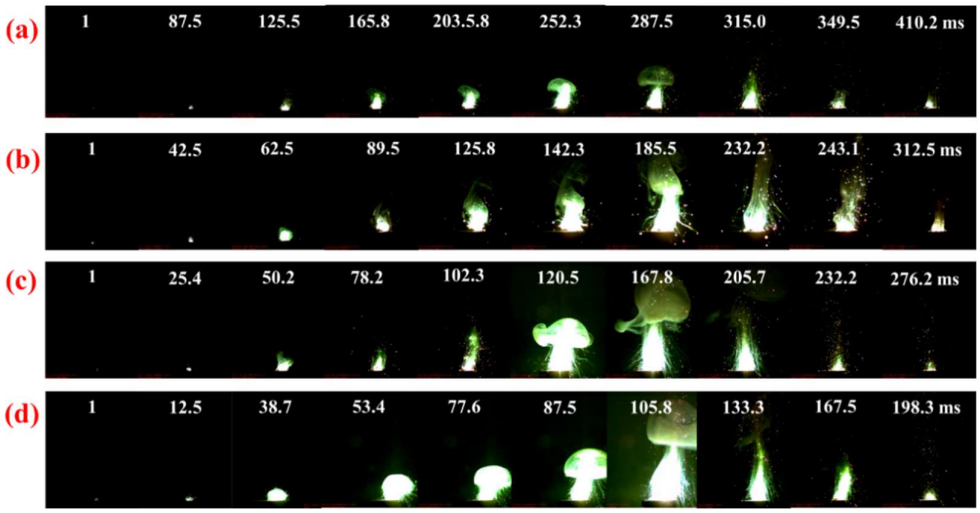


Figure 11. Ignition process of samples: (**a**) AlB_2/KP, (**b**) AlB_2@HTPFA-5/KP, (**c**) AlB_2@HTPFA-10/KP, (**d**) AlB_2@HTPFA-15/KP.

It was crucial to note that laser ignition combustion test findings were different from those of combustion in a confined environment. The former was performed with the condition of adding oxygen in a restricted region, and the later was achieved with the condition of adding oxidant in an open area. It was found that during the ignition of AlB_2@HTPFA, the confined region might prevent the diffusion of AlB_2 particles. A portion of the poorly permeabilized decomposition products would stay on the AlB_2 surface and impede the burning of AlB_2 particles, causing the decrease in reactivity with the increasing coating concentration.

To investigate the effect of AlB_2@HTPFA on the combustion process further, the products were collected and studied by XRD (Figure 12). It was revealed that the products were predominantly composed of Al_2O_3, B_2O_3, $KAlCl_4$, and $Al_4B_2O_9$. It was found that AlB_{12} was present in the product of AlB_2/KP due to the existence of HTPFA, while AlB_{12} was absent from the product of AlB_2@HTPFA-10/KP. AlB_{12} was an intermediate product of AlB_2 in the high-temperature oxidation process, indicating that mixed with KP, the reaction of AlB_2@HTPFA in the rapid ignition process was more complete than that of AlB_2.

Consequently, the ignition and combustion enhancement mechanism of AlB_2 coated with HTPFA was proposed. It could be concluded that during the burning of AlB_2@HTPFA-10/KP powder, the HTPFA on the surface broke down and reacted quickly, and the gas products' HF reacted with the oxide shell on the surface of AlB_2, generating a significant quantity of gas [6,58]. A pre-ignition reaction was obtained in this stage. The HF gas encouraged the diffusion of AlB_2 particles and the interaction between AlB_2 and KP, which could accelerate the combustion reaction of the composite fuel. As shown in Figure 11, high contents of HTPFA in AlB_2@HTPFA-10/KP are beneficial for enhancing combustion rates. Additionally, the high combustion performance of AlB_2 was obtained by adding the functionalized fluoropolymer.

That was of great significance to designing and fabricating AlB_2@functionalized fluoropolymer towards the potential application in high-energy propellant.

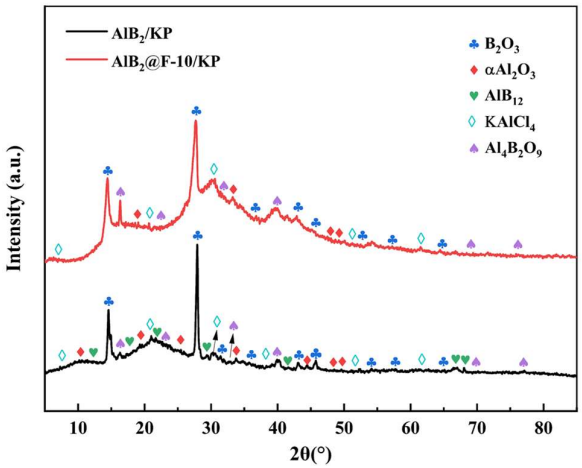


Figure 12. X-ray diffraction patterns of AlB_2/KP and AlB_2@HTPFA-10/KP.

4. Conclusions

In this study, AlB_2 coated with different contents (5 wt%, 10 wt%, and 15 wt%) of the HTPFA polymer was prepared. According to SEM, EDS, and particle size distribution analyses, the F element distributed uniformly on the surface of AlB_2@HTPFA, and the particles dispersed evenly without noticeable agglomeration. The results of XRD and XPS analysis demonstrated that HTPFA polymer adheres to the surface of AlB_2 particles. According to the thermal investigation, the oxidation peak temperature of samples increased as the amount of fluorine polymer increased. The results of combustion heat release indicated that AlB_2@HTPFA-5 releases more energy than AlB_2, and the combustion efficiency is increased by 4.1%. Meanwhile, the reactivity of AlB_2@HTPFA-5 was 0.65 MPa/s, which is ~1.5 times that of AlB_2. The ignition measurement illustrated that the pre-ignition interaction of the HTPFA polymer with surface oxide could accelerate the reaction and promote combustion efficiency. As a result, coating AlB_2 with HTPFA polymer is a potential approach for regulating the ignition and combustion characteristics of AlB_2 fuel, providing a viable way for the further application of AlB_2 as a fuel in energetic materials.

Supplementary Materials: The following supporting information can be downloaded at: https://www.mdpi.com/article/10.3390/ma18071452/s1, Table S1: EDS results; Figure S1: DSC/TG curves of HTPFA (Heating rate: 10 °C/min under air atmosphere); Table S2: Thermodynamic Parameters of Samples; Table S3: Compatibility of AlB_2@HTPFA-10 with Contact Materials; Figure S2: First light times for the 9 different boron-PTFE mixtures are shown. Four experiments were conducted for each condition using 200 W/cm^2; Figure S3: Images recorded from high speed video. Image A: PM1 (7.5 wt% PTFE); Image B: MM2 (15 wt% PTFE); Images C: PM3 (30 wt% PTFE); Image D: MM3 (30 wt% PTFE); Figure S4: Ignition process of samples: (a) AlB_2/KP (b) AlB_2@HTPFA-5/KP (c) AlB_2@HTPFA-10/KP (d) AlB_2@HTPFA-15/KP [30].

Author Contributions: Conceptualization, J.W. and Q.J.; Methodology, W.Z. and C.S.; Validation, J.W., C.S. and Y.O.; Formal Analysis, W.Z. and Q.J.; Investigation, J.W.; Resources, Y.O.; Data Curation, J.W. and W.Z.; Writing—Original Draft Preparation, J.W.; Writing—Review and Editing, W.Z.; Supervision, Q.J.; Project Administration, Q.J. All authors have read and agreed to the published version of the manuscript.

Funding: This research work was supported by the National Natural Science Foundation of China (Grant No. 22105067).

Institutional Review Board Statement: Not applicable.

Informed Consent Statement: Not applicable.

Data Availability Statement: The original contributions presented in this study are included in the article. Further inquiries can be directed to the corresponding author.

Conflicts of Interest: The authors declare no conflict of interest.

References

1. Padwal, M.; Castaneda, D.; Natan, B. Hypergolic combustion of boron-based propellants. *Proc. Combust. Inst.* **2021**, *38*, 6703–6711. [CrossRef]
2. Korotkikh, A.G.; Arkhipov, V.A.; Slyusarsky, K.V.; Sorokin, I.V. Study of Ignition of High-Energy Materials with Boron and Aluminum and Titanium Diborides. *Combust. Explos. Shock. Waves* **2018**, *54*, 350–356. [CrossRef]
3. Sivan, J.; Haas, Y.; Grinstein, D.; Kochav, S.; Yegudayev, G.; Kalontarov, L. Boron particle size effect on B/KNO_3 ignition by a diode laser. *Combust. Flame* **2015**, *162*, 516–527. [CrossRef]
4. Zhou, S.; Zhou, X.; Tang, G.; Guo, X.; Pang, A. Differences of thermal decomposition behaviors and combustion properties between CL-20-based propellants and HMX-based solid propellants. *J. Therm. Anal. Calorim.* **2020**, *140*, 2529–2540. [CrossRef]
5. Chintersingh, K.L.; Nguyen, Q.; Schoenitz, M.; Dreizin, E.L. Combustion of boron particles in products of an air–acetylene flame. *Combust. Flame* **2016**, *172*, 194–205. [CrossRef]
6. Deng, P.; Chen, P.; Fang, H.; Liu, R.; Guo, X. The combustion behavior of boron particles by using molecular perovskite energetic materials as high-energy oxidants. *Combust. Flame* **2022**, *241*, 112118. [CrossRef]
7. Dayanand, S.; Boppana, S.B.; Hemanth, J.; Telagu, A. Microstructure and corrosion characteristics of in situ aluminum diboride metal matrix composites. *J. Bio-Tribo-Corros.* **2019**, *5*, 1–10. [CrossRef]
8. Kenawy, S.H. Synthesis and Characterization of Aluminum Borate Ceramic Whiskers. *Int. J. Appl. Ceram. Technol.* **2011**, *8*, 783–792. [CrossRef]
9. Wang, X.; Liu, R.; He, Y.; Fu, Y.; Wang, J.; Li, A.; Guo, X.; Wang, M.; Guo, W.; Zhang, T. Determination of detonation characteristics by laser-induced plasma spectra and micro-explosion dynamics. *Opt. Express* **2022**, *30*, 4718–4736. [CrossRef]
10. Yanovskii, L.S.; Varlamova, N.I.; Borodako, P.V.; Popov, I.M. On influence of energy-producing additives upon the service characteristics of aviation fuels. *Russ. Aeronaut.* **2013**, *56*, 314–318. [CrossRef]
11. Weast, R.C.; Astle, M.J.; Beyer, W.H.; Company, C.R.; Selby, S.M.; Lide, D.R.; Frederikse, H.P.R.; Haynes, W.M.; Bruno, T.J. CRC handbook of chemistry and physics. *Am. J. Med. Sci.* **1982**, *257*, 423.
12. Liu, T.K.; Luh, S.P.; Perng, H.C. Effect of Boron Particle Surface Coating on combustion of solid propellants for ducted rockets. *Propellants Explos. Pyrotech.* **2010**, *16*, 156–166. [CrossRef]
13. Vellaisamy, U.; Biswas, S. Effect of metal additives on neutralization and characteristics of AP/HTPB solid propellants. *Combust. Flame* **2021**, *234*, 111627. [CrossRef]
14. Pang, W.; Fan, X.; Zhang, W.; Xu, H.; Li, J.; Li, Y.; Shi, X.; Li, Y. Application of Amorphous Boron Granulated with Hydroxyl-Terminated Polybutadiene in Fuel-Rich Solid Propellant. *Propellants Explos. Pyrotech.* **2011**, *36*, 360–366. [CrossRef]
15. Lyu, J.Y.; Chen, S.; He, W.; Zhang, X.; Tang, D.; Liu, P.; Yan, Q. Fabrication of High-Performance Graphene Oxide doped PVDF/CuO/Al Nanocomposites via Electrospinning. *Chem. Eng. J.* **2019**, *368*, 129–137. [CrossRef]
16. Yang, Y.; Zhao, F.; Xu, H.; Pei, Q.; Jiang, H.; Yi, J.; Xuan, C.; Chen, S. Hydrogen-enhanced combustion of a composite propellant with ZrH_2 as the fuel. *Combust. Flame* **2018**, *187*, 67–76. [CrossRef]
17. Ma, X.; Li, Y.; Hussain, I.; Yang, G.; Zhang, K. Core–Shell Structured Nanoenergetic Materials: Preparation and Fundamental Properties. *Adv. Mater.* **2020**, *32*, 2001291. [CrossRef]
18. He, W.; Li, Z.H.; Chen, S.; Yang, G.; Yang, Z.; Liu, P.; Yan, Q. Energetic Metastable n-Al@PVDF/EMOF Composite Nanofibers with Improved Combustion Performances. *Chem. Eng. J.* **2019**, *41*, 123146. [CrossRef]
19. Zhu, Y.; Zhou, X.; Wu, C.; Cheng, H.; Lu, Z.; Zhang, K. Si Wire Supported MnO_2/Al/Fluorocarbon 3D Core/Shell Nanoenergetic Arrays with Long-Term Storage Stability. *Chin. Ophthalmic Res.* **2017**, *7*, 6678. [CrossRef]
20. Deng, S.; Jiang, Y.; Huang, S.; Shi, X.; Zhao, J.; Zheng, X. Tuning the morphological, ignition and combustion properties of micron-Al/CuO thermites through different synthesis approaches. *Combust. Flame* **2018**, *195*, 303–310. [CrossRef]
21. Li, X.; Huang, C.; Yang, H.; Li, Y.; Cheng, Y. Thermal reaction properties of aluminum/copper (II) oxide/poly(vinylidene fluoride) nanocomposite. *J. Therm. Anal. Calorim.* **2016**, *124*, 899–907.
22. DeLisio, J.B.; Hu, X.; Wu, T.; Egan, G.C.; Young, G.; Zachariah, M.R. Probing the Reaction Mechanism of Aluminum/Poly(vinylidene fluoride) Composites. *J. Phys. Chem. B* **2016**, *120*, 5534–5542. [CrossRef] [PubMed]
23. He, W.; Liu, P.; He, G.; Gozin, M.; Yan, Q. Highly Reactive Metastable Intermixed Composites (MICs): Preparation and Characterization. *Adv. Mater.* **2018**, *30*, 1706293. [CrossRef]
24. Wang, H.; Rehwoldt, M.; Kline, D.J.; Wu, T.; Wang, P.; Zachariah, M.R. Comparison study of the ignition and combustion characteristics of directly-written Al/PVDF, Al/Viton and Al/THV composites. *Combust. Flame* **2019**, *201*, 181–186. [CrossRef]

25. Young, G.; Stoltzi, C.A.; Mayo, D.H.; Roberts, C.W.; Milby, C.L. Combustion Behavior of Solid Fuels Based on PTFE/Boron Mixtures. *Combust. Sci. Technol.* **2013**, *185*, 1261–1280. [CrossRef]
26. Pang, W.Q. *Boron-Based Fuel-Rich Propellant: Properties, Combustion and Technology Aspects*; Taylor & Francis Group: Abingdon, UK; CRC Press: Boca Raton, FL, USA, 2019.
27. Keerthi, V.; Nie, H.; Pisharath, S.; Hng, H.H. Combustion characteristics of fluoropolymer coated boron powders. *Combust. Sci. Technol.* **2020**, *194*, 1183–1198. [CrossRef]
28. Ulas, A.; Kuo, K.K.; Gotzmer, C. Ignition and combustion of boron particles in fluorine-containing environments. *Combust. Flame* **2001**, *127*, 1935–1957. [CrossRef]
29. Young, G.; Roberts, C.W.; Stoltz, C.A. Ignition and combustion enhancement of boron with polytetrafluoroethylene. *J. Propuls. Power* **2015**, *31*, 386–392. [CrossRef]
30. Hedman, T.D.; Demko, A.R.; Kalman, J. Enhanced ignition of milled boron-polytetrafluoroethylene mixtures. *Combust. Flame* **2018**, *198*, 112–119. [CrossRef]
31. Jiang, Y.; Demko, A.R.; Baek, J.; Shi, X.; Vallez, L.; Ning, R.; Zheng, X. Facilitating laser ignition and combustion of boron with a mixture of graphene oxide and graphite fluoride. *Appl. Energy Combust. Sci.* **2020**, *1*, 100013. [CrossRef]
32. Xu, Y.; Cui, Q.Z.; Zhao, C.W. Liquid phase in-situ synthesis of LiF coated boron powder composite and performance study. *Def. Technol.* **2020**, *16*, 635–641. [CrossRef]
33. Zhou, T.; Li, X.; Liu, C.; Shi, X.; Wu, B.; Duan, X.; Yang, G. Butterfly wing fans the fire: High efficient combustion of CWs/CL-20/AP nanocomposite for light ignited micro thruster using multi-channeled hierarchical porous structure from butterfly wing scales. *Combust. Flame* **2021**, *231*, 111505. [CrossRef]
34. Cheng, L.; Yang, H.; Yang, Y.; Li, Y.; Meng, Y.; Li, Y.; Song, D.; Chen, H.; Artiaga, R. Preparation of B/Nitrocellulose/Fe particles and their effect on the performance of an ammonium perchlorate propellant—ScienceDirect. *Combust. Flame* **2020**, *211*, 456–464. [CrossRef]
35. Yan, L.; Zhu, B.; Chen, J.; Sun, Y. Study on nano-boron particles modified by PVDF to enhance the combustion characteristics. *Combust. Flame* **2023**, *248*, 112556. [CrossRef]
36. Tang, W.; Zeng, T.; Hu, J.; Li, J.; Yang, R. Investigation on the thermal decomposition of the elastomer containing fluoroolefin segment by DSC-TG-MS-FTIR. *Polym. Adv. Technol.* **2021**, *32*, 4880–4890. [CrossRef]
37. Ge, Z.; Zhang, X.; Dai, J.; Li, W.; Luo, Y. Synthesis, characterization and properties of a novel fluorinated polyurethane. *Eur. Polym. J.* **2009**, *45*, 530–536. [CrossRef]
38. Wang, X.; Xu, J.; Li, L.; Liu, Y.; Li, Y.; Dong, Q. Influences of fluorine on microphase separation in fluorinated polyurethanes. *Polymer* **2016**, *98*, 311–319. [CrossRef]
39. Wen, J.; Sun, Z.; Xiang, J.; Fan, H.; Chen, Y.; Yan, J. Preparation and characteristics of waterborne polyurethane with various lengths of fluorinated side chains. *Appl. Surf. Sci.* **2019**, *494*, 610–618. [CrossRef]
40. Cobranchi, D.P.; Botelho, M.; Buxton, L.W.; Buck, R.C.; Kaiser, M.A. Vapor pressure determinations of 8-2 fluorortelomer alcohol and 1-H perfluorooctane by capillary gas chromatography: Relative retention time versus headspace methods. *J. Chromatogr. A* **2006**, *1108*, 248–251. [CrossRef]
41. Silva, G.M.C.; Morgado, P.; Haley, J.D.; Montoya, V.M.T.; McCabe, C.; Martins, L.F.G.; Filipe, E.J.M. Vapor pressure and liquid density of fluorinated alcohols: Experimental, simulation and GC-SAFT-VR predictions. *Fluid Phase Equilibria* **2016**, *425*, 297–304. [CrossRef]
42. Ou, Y.; Sun, Y.; Jiao, Q. Properties related to linear and branched network structure of hydroxyl terminated polybutadiene. *e-Polymers* **2018**, *18*, 267–274. [CrossRef]
43. Ma, M.; Kwon, Y. Preparation of energetic polyurethane binders with enhanced properties by nonmigratory reactive monocyclic plasticizers. *Eur. Polym. J.* **2019**, *123*, 109414. [CrossRef]
44. Shimada, S. Thermosonimetry and thermomicroscopy of the decomposition of $NaClO_4$ and $KClO_4$. *J. Therm. Anal.* **1993**, *40*, 1063–1068. [CrossRef]
45. Lee, J.-S. Thermal properties and firing characteristics of the Zr/$KClO_4$/Viton A priming compositions. *Thermochim. Acta* **2002**, *392*, 147–152. [CrossRef]
46. Tan, L.; Lu, X.; Liu, N.; Yan, Q. Further enhancing thermal stability of thermostable energetic derivatives of dibenzotetraazapentene by polydopamine/graphene oxide coating. *Appl. Surf. Sci.* **2021**, *543*, 148825. [CrossRef]
47. Trunov, M.A.; Schoenitz, M.; Zhu, X.; Dreizin, E.L. Effect of polymorphic phase transformations in Al_2O_3 film on oxidation kinetics of aluminum powders. *Combust. Flame* **2005**, *140*, 310–318. [CrossRef]
48. Shang, Y.; Chen, S.; Yu, Z.; Huang, R.; He, C.; Ye, Z.; Zhang, W.; Chen, X. Silver(I)-based molecular perovskite energetic compounds with exceptional thermal stability and energetic performance. *Inorg. Chem.* **2022**, *61*, 4143–4149. [CrossRef]
49. Noor, F.; Zhang, H.; Korakianitis, T.; Wen, D. Oxidation and ignition of aluminum nanomaterials. *Phys. Chem. Chem. Phys. PCCP* **2013**, *15*, 20176–20188. [CrossRef]

50. Zhu, S.; Cao, X.; Cao, X.; Feng, Y.; Lin, X.; Han, K.; Li, X.; Deng, P. Metal-doped (Fe, Nd, Ce, Zr, U) graphitic carbon nitride catalysts enhance thermal decomposition of ammonium perchlorate-based molecular perovskite. *Mater. Des.* **2021**, *199*, 109426. [CrossRef]
51. Yan, T.; Liu, P.; Song, N.; Liu, J.; Ou, Y. Thermally active nano-aluminum particles with improved flowability prepared by adsorbing multi-component layer. *Combust. Flame* **2021**, *234*, 111680. [CrossRef]
52. Hall, A.; Economy, J. The Al (L) + AlB_{12} AlB_2 peritectic transformation and its role in the formation of high aspect ratio AlB2 flakes. *J. Phase Equilibria* **2000**, *21*, 63–69. [CrossRef]
53. Velasco, F.; Guzman, S.; Moral, C.; Bautista, A. Oxidation of micro-sized aluminium particles: Hollow alumina spheres. *Oxid. Met.* **2013**, *80*, 403–422. [CrossRef]
54. Blackburn, P.E.; Büchler, A.; Stauffer, J.L. Thermodynamics of Vaporization in the Aluminum Oxide—Boron Oxide System1a. *J. Phys. Chem.* **1966**, *70*, 2469–2474. [CrossRef]
55. Nagai, T.; Ogasawara, Y.; Maeda, M. Thermodynamic measurement of (Al_2O_3 + B_2O_3) system by double Knudsen cell mass spectrometry. *J. Chem. Thermodyn.* **2009**, *41*, 1292–1296. [CrossRef]
56. Whittaker, M.L.; Sohn, H.Y.; Cutler, R.A. Oxidation kinetics of aluminum diboride. *J. Solid State Chem.* **2013**, *207*, 163–169. [CrossRef]
57. Crouse, C.A.; Pierce, C.J.; Spowart, J.E. Synthesis and reactivity of aluminized fluorinated acrylic (AlFA) nanocomposites. *Combust. Flame* **2012**, *159*, 3199–3207. [CrossRef]
58. Yan, T.; Liu, P.; Song, N.; Ou, Y. Insight into combustion characteristics of micro- and nano-sized boron carbide. *Combust. Flame* **2023**, *251*, 112721. [CrossRef]

Disclaimer/Publisher's Note: The statements, opinions and data contained in all publications are solely those of the individual author(s) and contributor(s) and not of MDPI and/or the editor(s). MDPI and/or the editor(s) disclaim responsibility for any injury to people or property resulting from any ideas, methods, instructions or products referred to in the content.